Comparing and optimizing analytical, numerical and experimental vibration models for a simply-supported ribbed plate

James Akl*, Fadi Alladkani, Patrick Dumond

Department of Mechanical Engineering, University of Ottawa, 161 Louis Pasteur, CBY A208, Ottawa, Canada K1N 6N5

Abstract

Ribbed plates are common components in aircrafts, ships, and structures. Due to safety considerations and proper functioning, it is important to predict the natural frequencies and mode-shapes of such systems. There are many analytical, numerical, and experimental methods that extract the modal parameters of ribbed plates. However, each present advantages and tradeoffs. The aim of this paper is to implement some of the most common modeling and experimental approaches, optimize them wherever possible, and compare their strengths and weaknesses. The different instances of the analytical model are based on the assumed-modes method and differ only their geometric configuration and trial function selection, in order to observe the effects of each. The numerical model is a finite element analysis of the ribbed plate employing higher-order shear theories. Two experiments are performed to validate and optimize the models, and to weigh the benefits of the two common setups. An in-depth implementation of the analytical model demonstrates the use of parallelization and concurrency, mathematical simplifications, and algorithmic improvements in order to optimize performance. The parallelized program is then put through algorithmic analysis to estimate its local order of growth and study its running time. By comparing the performance, accuracy, simplicity, stability, affordability, and parametrization potential of the studied approaches, vibration scientists and engineers are able to better select the method suitable for their research, application, or design.

Keywords:
Ribbed-plate system
Simply-supported vibrations
Assumed-modes method
Finite elements method
Experimental modal analysis

* Corresponding author.
E-mail addresses: james.akl@lau.edu (J. Akl), fadi.alladkani@lau.edu (F. Alladkani), pdumond@uottawa.ca (P. Dumond).

1. Introduction

The reinforcement of plates through the use of ribs arises in diverse and practical engineering applications such as those found in the industrial, structural, automotive, aerospace, and naval sectors. Ribs are added to modify either the structural behavior of the plate (e.g. strengthening) or its dynamical behavior (e.g. offsetting its resonance point). In applications where, variable loads are applied to ribbed plates, or when subjected to vibratory motion, it is often crucial to perform modal analysis to estimate the natural frequencies and mode-shapes of the system. Such knowledge enables a more detailed design, taking into account safety considerations, which helps prevent high-amplitude vibrations from causing system failure.

There exists a vast number of methods for approximating the natural frequencies and mode-shapes of ribbed plates. However, they all fall under analytical, numerical, or experimental approaches, including a combination of these. Analytical methods include variational techniques (Rayleigh-Ritz, Galerkin, assumed-modes, etc.) [1-7] that share global characteristics, while one of the dominant numerical approaches remains the finite element method [6], facilitated by the advancement of increasingly powerful computers. In parallel, certain experimental setups enable the extraction of modal parameters of a measured system. Though experimental setups can vary greatly from one instance to another, clear categories can nonetheless be drawn. On one hand there are methods that resemble impulse testing [7-9], whereby embedded accelerometers output signals to be processed using well-known algorithms. On the other hand, there are optical methods that make use of Chaldni patterns [10] to examine mode-shapes and measure their corresponding natural frequencies. Of course, laser vibrometry has emerged as an excellent non-contact approach to vibration measurement, but remains out of reach for many researchers on a budget. While great research has significantly improved the methods described above, the best approach for any given situation is often unclear. Individuals are quick to favor one method over the other based on familiarity, but in reality, the optimal approach should depend on the desired outcome and the limitations of the problem or application.

In this paper, common methods for the analytical (assumed-modes), numerical (finite element), and experimental (impact hammer, Chladni patterns) will be thoroughly analyzed

and compared. The analytical method is formulated with variations in trial function selection, and in system configuration, based on those currently found in the literature [11-15]. The effects of each on the modal results are examined. Thorough implementation details will be given, as well as multiple performance optimizations (parallelization and concurrency, mathematical simplifications and algorithmic improvements). Moreover, an algorithmic analysis on the analytical implementation is performed to estimate the local order of growth of its running time. For the numerical approach, both formulation and implementation details are provided for a fair comparison against the analytical models. Finally, two separate experiments are performed on a dedicated aluminum ribbed plate fabricated to closely match the mathematical models. The setups for the impact hammer test and the Chladni pattern method are outlined in detail and their respective advantages and limitations are highlighted. These experiments not only demonstrate common experimental modal analysis techniques, but also provide a benchmark against which the mathematical models can be compared and validated. Finally, the various methods are compared in terms of accuracy, performance, stability, simplicity, ease of parametrization, and affordability where applicable. The resulting data will prove to be useful to vibration scientists and engineers in evaluating the appropriate method best suited for their research, application or design problem.

2. Models and Methods

The objective is to perform modal analysis to determine the natural frequencies and mode-shapes, of a rectangular ribbed plate. Three main approaches present themselves, each with their own methods: numerical simulations (the finite element method), analytical modeling (approximate methods and variational techniques), and experimental verification (performing physical measurements to determine vibrational modal outputs).

2.1. System description

2.1.1. Plate parameters

The geometrical parameters of the plate are shown in Fig. 1.1 where a, b, and h are the length, width, and thickness of the base plate, respectively. L_r and h_r are the length and thickness of the rib, respectively. The starting and ending abscissa of the rib are $c_1 = (a - L_r)/2$ and $c_2 = (a + L_r)/2$, respectively. Additionally, the material properties are: Poisson's ratio ν, Young's modulus E, and the volumetric mass density μ.

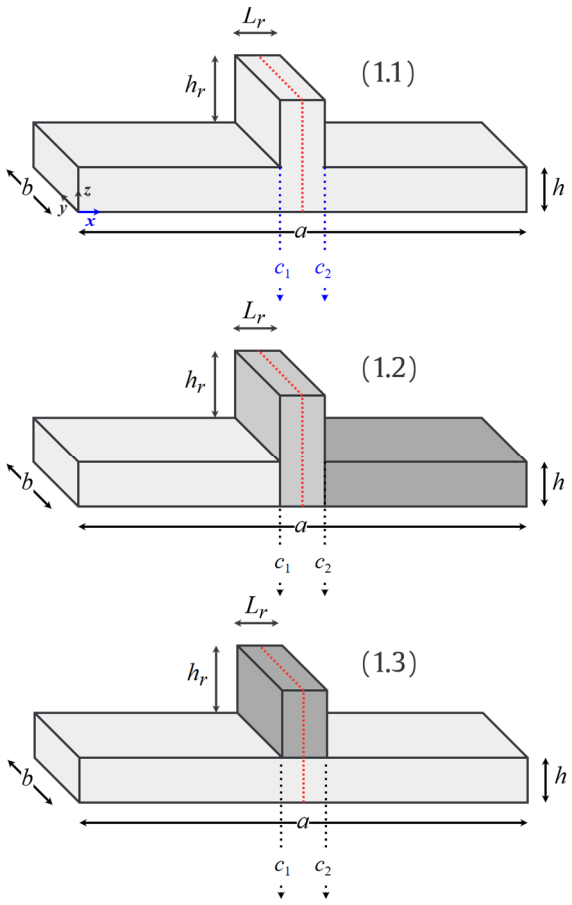

Fig. 1. Geometrical parameters of the ribbed plate and modeling configurations.

2.1.2. Common assumptions

It is assumed that the modeled plate is perfectly simply-supported. However, corresponding plates in engineering applications have mixed boundary conditions (between simply-supported and clamped). Moreover, since damping is neglected, the system is considered to be conservative. Effectively, since the study seeks no further than the first five natural frequencies, then dissipative effects are small and become considerable only at higher frequencies. Finally, the material used is assumed to be isotropic.

2.2. Numerical model

The finite element method (FEM) model is formulated and simulated on COMSOL 5.1 and is the most developed model in terms of complexity. It uses higher-order shear deformation theories well-described in [16]. The formulation uses the Cartesian coordinate system (x, y, z)

whose origin is the centroid of the base plate and where z is the direction normal to the surface of the plate.

2.2.1. Base and augmented models

The governing dynamic equation used to extract the natural frequencies ω is

$$-\mu\omega^2\mathbf{u} = \nabla \cdot \sigma + \mathbf{F} + 6(\mathbf{M} \times \mathbf{n})\frac{z}{h^2} \tag{1}$$

Where $\mathbf{u}$ is the mid-surface linear displacement vector, σ the Second Piola-Kirchhoff stress tensor, $\mathbf{F}$ and $\mathbf{M}$ the net force and moment vectors, and $\mathbf{n}$ the normal unit vector.

The bending σ_b, membrane σ_m, and shearing σ_s parts of the stress tensor σ can be expanded as follows:

$$\sigma_b = \sigma_0 + \sigma_{\text{ext}} + \sigma_d + \frac{h}{2}\mathbf{C}\,(\chi - \chi_0) \tag{2}$$

$$\sigma_m = \sigma_0 + \sigma_{\text{ext}} + \sigma_d + \mathbf{C}\,(\gamma - \gamma_0) \tag{3}$$

$$\sigma_s = \sigma_0 + \sigma_{\text{ext}} + \sigma_d + 2\kappa G\,(\zeta - \zeta_0) \tag{4}$$

Where σ_0 is the initial stress, σ_{ext} the external stress, σ_d the deviatoric stress, $\mathbf{C}$ the elasticity matrix (whose terms are functions of E and ν), G the modulus of rigidity, $\kappa = 5/6$ the shear correction factor, χ the element covariant membrane tensor, γ the element covariant bending tensor, ζ the element covariant transverse shear, and $\{\chi_0, \gamma_0, \zeta_0\}$ their initial values.

Simply supported boundary conditions are added using the four equalities $\{\mathbf{u}\cdot\mathbf{n} = \mathbf{0}, \mathbf{u}\cdot\mathbf{t} = \mathbf{0}, \mathbf{u}\cdot(\mathbf{t}\times\mathbf{n}) = \mathbf{0}, \mathbf{t}\cdot\mathbf{s} = \mathbf{0}\}$ where $\mathbf{t}$ is the tangent unit vector and $\mathbf{s}$ the displacement of shell normals. In addition, the in-plane stress is $\sigma_{\text{inplane}} = \sigma_m + z\sigma_b$ and $\sigma_z = 0$ for $-h/2 \le z \le h/2$

In order to better match the impulse hammer experimental configuration discussed below, two point-masses are added in the locations of the two accelerometers used on the plate. This augmented model is used to match the experiment, while the base model is used to obtain values without the addition of accelerometers. The force and moment added by each accelerometer of mass m_{acc} are $\mathbf{F}_{acc} = (i\,\alpha - \omega)\omega m_{acc}\,\mathbf{u}$ and $\mathbf{M}_{acc} = (i\,\alpha - \omega)\omega\mathbf{J}\,\boldsymbol{\theta}$, where $\boldsymbol{\theta} = \mathbf{n}\times\mathbf{s}$ is the angular displacement vector, α the mass damping parameter, $\mathbf{J}$ the mass moment of inertia matrix, and i the imaginary number.

2.2.2. Discretization

The model uses triangular shell elements in a quadratic displacement field. Both the displacement field and the displacement of shell normals are complex-valued. The system uses an adaptive mesh, as in Fig. 2, with a maximum element size of $4.12 \cdot 10^{-3}$ m, a minimum element size of $1.55 \cdot 10^{-5}$ m, a maximum element growth rate of 1.2, a curvature factor of 0.25, and a narrow region resolution of 1. The mesh gets increasingly finer near the rib, where the effects have a higher impact on the results.

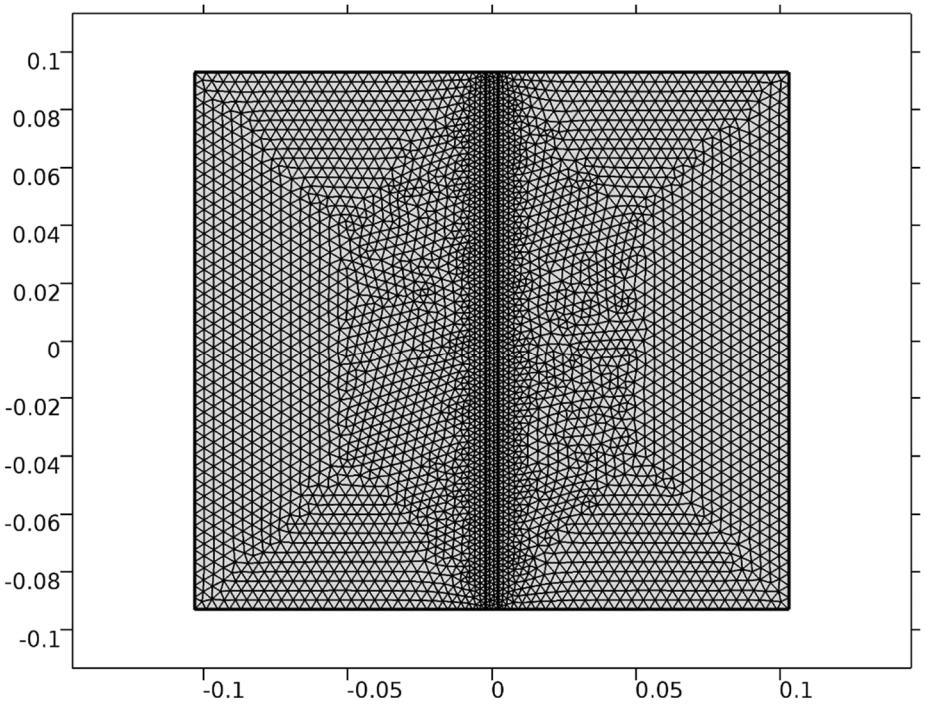

Fig. 2. Discretization of the plate using an adaptive mesh.

2.3. Analytical models

The analytical models exploit a symbolic approach for obtaining the natural frequencies and mode-shapes of the plate. The assumed-modes method (AMM) is used and is well-formulated in [17]. AMM was chosen because it allows using: (1) energy formulations of the model that abstracts away geometrical complexities, (2) flat plate and beam solutions and their corresponding mode-shapes as the fundamental elements (individual trial functions) of the analytical solutions, and (3) a constructed global solution as opposed to the dispersed local solutions provided by FEM. The advantage and flexibility of AMM lies in its parametric and symbolic solutions, which enables the modal analysis of plates with changing parameters and

rapid numerical solutions. Its elegance consists of solving the governing PDEs only once, and producing a reusable multivariate solution. The system can be modeled using three different approaches, whereas the rib is modeled as either: (1) a taller section of the base plate (*Rib* ⊂ *Plate*, Fig. 1.2), (2) a superimposed flat rectangular plate (*Rib* ≡ *Plate*, Fig. 1.3), and (3) a superimposed flat rectangular beam (*Rib* ≡ *Beam*, Fig. 1.3). Additionally, since a variational approach will be used, the choice of trial functions (harmonic or polynomial) will be important.

2.3.1. Model assumptions

Kirchhoff–Love plate theory is used and is developed based on specific assumptions: (1) straight lines orthogonal to the mid-surface pre-deformation remain straight post-deformation, (2) straight lines orthogonal to the mid-surface pre-deformation remain orthogonal post-deformation, and (3) plate thickness is constant throughout deformation. To be clear, the mid-surface curvature starts null and must end null after deformation, i.e. the xy-planar cross-section of the plate at exactly half its thickness must restore to its flat shape after deformation. In simpler terms, these assumptions require linear elastic deformation, valid in thin plates subject to relatively small forces. In fact, the model was adjusted to experiments performed on a plate with small thickness-to-width ratios, and which was subjected to forces no greater than 100 N. Since deflections are small compared to the thickness, the normal, transverse, shear, and torsional stresses are neglected. These assumptions enable practical use of the model but induce noticeable errors near the thicker ribbed region.

2.3.2. General formulation

The end-goal of the analysis is to obtain the modal parameters: the natural frequencies ω and mode-shapes $\mathbf{U}$. To make this possible, certain preliminary definitions are required.

The transverse displacement $w(t,x,y)$ is defined as a weighting function, composed of individual trial functions $\phi_{i,j}(x,y)$ as weights to the generalized coordinates $q_{i,j}(t)$.

$$w(t,x,y) = \sum_{j=1}^{n} \sum_{i=1}^{n} \phi_{i,j}(x,y) \cdot q_{i,j}(t) \tag{5}$$

The preset index n controls the number of individual trial functions used, the result of which is n^2 trial functions (n trial functions in each of the x and y directions). As part of calculus of variations, more trial functions generally improve the accuracy of the solutions, since most variational methods converge to exact solutions as the input n grows asymptotically. This is particularly true with the assumed-modes method.

The formulation assumes an arbitrary form for the individual trial functions. In effect, the different options (harmonic, polynomial, combined) will have a significant impact on the model behavior.

The continuous system is described by generalized coordinates $q_{i,j}(t)$ both in matrix or vector forms,

$$\mathbf{Q} = \left(q_{i,j}\right)_{1 \le i,j \le n} \in \mathbb{R}^{n \times n} \quad \Longrightarrow \quad \mathbf{q} = \mathrm{vec}\left(\mathbf{Q}^{\mathrm{T}}\right) = (q_i)_{1 \le i \le n^2} \in \mathbb{R}^{n^2} \tag{6}$$

and by the mass and stiffness matrices of the system.

$$\mathbf{M} = \left(m_{i,j}\right)_{1 \le i,j \le n^2} \in \mathbb{R}^{n^2 \times n^2} \qquad \mathbf{K} = \left(k_{i,j}\right)_{1 \le i,j \le n^2} \in \mathbb{R}^{n^2 \times n^2} \tag{7}$$

Essentially, it is known that the desired modal outputs (natural frequencies and mode-shapes) are obtained by solving the generalized eigenvalue and eigenvector problems:

$$\begin{cases} \det(\mathbf{K} - \boldsymbol{\lambda}\,\mathbf{M}) = 0 \\ (\mathbf{K} - \boldsymbol{\lambda}\,\mathbf{M})\,\mathbf{A} = 0 \end{cases} \tag{8}$$

Where $\boldsymbol{\lambda} \in \mathbb{R}^{n^2 \times n^2}$ and $\mathbf{A} \in \mathbb{R}^{n^2 \times n^2}$ are the eigenvalue and eigenvector matrices, respectively, and are used to compute the natural frequencies $\boldsymbol{\omega}$ and mode-shapes $\mathbf{U}$.

The natural frequency vector is simply the square root map of the eigenvalue matrix's diagonal.

$$\boldsymbol{\omega} = \left(\sqrt{\lambda_{i,i}}\right)_{1 \le i \le n^2} \in \mathbb{R}^{n^2} \tag{9}$$

The mode-shapes vector contains linear combinations of individual trial functions,

$$\mathbf{U} = \mathbf{A}\,\boldsymbol{\Phi} = \left(u_i(x,y)\right)_{1 \le i \le n^2} = \left(\sum_{j=1}^{n^2} a_{i,j}\,\phi_i(x,y)\right)_{1 \le i \le n^2} \in \mathbb{R}^{n^2} \tag{10}$$

where the trial functions vector $\mathbf{\Phi}$ is obtained from the trial functions matrix.

$$\mathbf{\Phi} = \mathrm{vec}\left[\left(\phi_{i,j}\right)^{\mathrm{T}}_{1 \le i,j \le n}\right] = (\phi_i)_{1 \le i \le n^2} \in \mathbb{R}^{n^2} \tag{11}$$

With the preliminaries defined, the Euler-Lagrange equation offers an energy description of the system,

$$\frac{\mathrm{d}}{\mathrm{d}t}\left(\frac{\partial L}{\partial \dot{\mathbf{q}}}\right) - \frac{\partial L}{\partial \mathbf{q}} = \mathbf{f} \Longrightarrow \frac{\mathrm{d}}{\mathrm{d}t}\left(\frac{\partial T}{\partial \dot{\mathbf{q}}}\right) + \frac{\partial V}{\partial \mathbf{q}} = \mathbf{0} \tag{12}$$

where $L = T - V$ is the Lagrangian, subtracting the kinetic energy T from the potential energy V of the system and $\mathbf{f} = (f_i)_{1 \le i \le n^2} \in \mathbb{R}^{n^2}$ is the external load factor. Here, the system assumes free vibration and as such $\mathbf{f} = \mathbf{0}$. The mathematical context of these variational techniques is elaborated in [18].

The equation reduces to $\mathbf{M\ddot{q}} + \mathbf{Kq} = \mathbf{0}$ and can be rewritten as:

$$\frac{\mathrm{d}}{\mathrm{d}t}\boldsymbol{\delta}_\mathbf{1} + \boldsymbol{\delta}_\mathbf{2} = \mathbf{0} \Leftrightarrow \left(\boldsymbol{\delta}_\mathbf{1} = \frac{\partial T}{\partial \dot{\mathbf{q}}} = \mathbf{M\dot{q}}\right) \wedge \left(\boldsymbol{\delta}_\mathbf{2} = \frac{\partial V}{\partial \mathbf{q}} = \mathbf{Kq}\right) \tag{13}$$

Or in matrix form, since the $q_{i,j}\,(t)$ in Eq. (6) are initially formed using matrices, rewritten as:

$$\frac{\mathrm{d}}{\mathrm{d}t}\boldsymbol{\Delta}_\mathbf{1} + \boldsymbol{\Delta}_\mathbf{2} = \mathbf{0} \Leftrightarrow \left(\boldsymbol{\Delta}_\mathbf{1} = \frac{\partial T}{\partial \dot{\mathbf{Q}}} = \mathbf{M\dot{Q}}\right) \wedge \left(\boldsymbol{\Delta}_\mathbf{2} = \frac{\partial V}{\partial \mathbf{Q}} = \mathbf{KQ}\right) \tag{14}$$

The mass and stiffness elements are obtained as follows. First $\boldsymbol{\Delta}_\mathbf{2}$ and $\boldsymbol{\Delta}_\mathbf{1}$ are developed by differentiating the potential and kinetic energies with respect to every generalized coordinate q and its first time-derivative $\dot{q}$, respectively. Second, these matrices are vectorized into $\boldsymbol{\delta}_\mathbf{1}$ and $\boldsymbol{\delta}_\mathbf{2}$ which contain linear combinations of the desired coefficients $m_{i,j}$ with $\dot{q}_j$ and $k_{i,j}$ with q_j. Finally, with $\boldsymbol{\delta}_\mathbf{1}$ and $\boldsymbol{\delta}_\mathbf{2}$ made explicit, the coefficients $m_{i,j}$ and $k_{i,j}$ are extracted to populate the matrices $\mathbf{M}$ and $\mathbf{K}$, respectively. Mathematically, this is written as:

$$\boldsymbol{\Delta}_1 = \left(\frac{\partial T}{\partial \dot{q}_{i,j}}\right)_{1 \le i,j \le n} \in \mathbb{R}^{n \times n} \quad \Longrightarrow \quad \boldsymbol{\delta}_\mathbf{1} = \mathrm{vec}\left(\boldsymbol{\Delta}_1^{\mathrm{T}}\right) = \left(\sum_{j=1}^{n^2} m_{i,j} \cdot \dot{q}_j\,(t)\right)_{1 \le i \le n^2} \in \mathbb{R}^{n^2} \tag{15}$$

$$\boldsymbol{\Delta_2} = \left(\frac{\partial V}{\partial q_{i,j}}\right)_{1 \le i,j \le n} \in \mathbb{R}^{n \times n} \quad \Longrightarrow \quad \boldsymbol{\delta_2} = \mathrm{vec}\left(\boldsymbol{\Delta}_2^{\mathrm{T}}\right) = \left(\sum_{j=1}^{n^2} k_{i,j} \cdot q_j\,(t)\right)_{1 \le i \le n^2} \in \mathbb{R}^{n^2} \tag{16}$$

This formulation is optimized for computer algebra systems, which first develop $\boldsymbol{\Delta_1}$ and $\boldsymbol{\Delta_2}$, then vectorize them into $\boldsymbol{\delta_1}$ and $\boldsymbol{\delta_2}$, and finally extract $\mathbf{M}$ and $\mathbf{K}$.

With the common procedures set in place, the plate can be parametrized so that the model's three configurations can each provide their own kinetic and potential energy definitions.

For compactness, the potential energy integrand $W_V(t,x,y)$ is defined as:

$$W_V(t,x,y) = \left(w_{xx} + w_{yy}\right)^2 + 2\,(1-\nu) \cdot \left(w_{xy}^2 - w_{xx}\,w_{yy}\right) \tag{17}$$

Where the subscripts denote partial derivatives in the given direction, as per standard notation.

All equations up to this point are common to all ribbed-plate configurations. The general formulation treats the kinetic and potential energy of individual plate sections as known. However, the details of each of the three configurations considered are provided as follows.

2.3.3. Configuration 1: Rib ⊂ Plate

The kinetic energy of the system is evaluated as the superposition each section of the plate (Fig. 1.2).

$$T = \frac{1}{2}\left(\int_0^{c_1}\int_0^{b} \rho_1 \cdot \dot{w}^2 \,\mathrm{d}y\;\mathrm{d}x + \int_{c_1}^{c_2}\int_0^{b} \rho_2 \cdot \dot{w}^2 \,\mathrm{d}y\;\mathrm{d}x + \int_{c_2}^{a}\int_0^{b} \rho_1 \cdot \dot{w}^2 \,\mathrm{d}y\;\mathrm{d}x\right) \tag{18}$$

Where $\rho_1 = \mu h$ and $\rho_2 = \mu(h + h_r)$ are the area mass densities of each section.

Likewise, for the potential energy.

$$V = \frac{1}{2}\left(\int_0^{c_1}\int_0^{b} d_1 \cdot W_V \,\mathrm{d}y\;\mathrm{d}x + \int_{c_1}^{c_2}\int_0^{b} d_2 \cdot W_V \,\mathrm{d}y\;\mathrm{d}x + \int_{c_2}^{a}\int_0^{b} d_1 \cdot W_V \,\mathrm{d}y\;\mathrm{d}x\right) + V_S \tag{19}$$

Where the flexural rigidities are given as:

$$d_1 = \frac{E\,h^3}{12\,(1-\nu^2)} \qquad d_2 = \frac{E\,(h+h_r)^3}{12\,(1-\nu^2)} \tag{20}$$

The term V_S is only added for generality. It corresponds to the elastic potential energy of the hypothetical massless springs present at the plate boundaries. The existence of these springs will depend on the type of trial functions used. Unless the penalty method is used, then V_S is null. The different cases will be elaborated upon in section 2.3.6.

2.3.4. Configuration 2: Rib ≡ Plate

This configuration treats the rib as another rectangular flat plate placed on top of the base plate (Fig. 1.3).

The kinetic energy of the system is evaluated as a superposition of both the base and top plates.

$$T = \frac{1}{2}\left(\int_0^a \int_0^b \rho_1 \cdot \dot{w}^2 \, \mathrm{d}y \, \mathrm{d}x + \int_{c_1}^{c_2} \int_0^b \rho_2 \cdot \dot{w}^2 \, \mathrm{d}y \, \mathrm{d}x\right) \tag{21}$$

Here $\rho_1 = \mu h$ and $\rho_2 = \mu h_r$.

Likewise, for the potential energy.

$$V = \frac{1}{2}\left(\int_0^a \int_0^b d_1 \cdot W_V \, \mathrm{d}y \, \mathrm{d}x + \int_{c_1}^{c_2} \int_0^b d_2 \cdot W_V \, \mathrm{d}y \, \mathrm{d}x\right) + V_S \tag{22}$$

Here the flexural rigidities are

$$d_1 = \frac{E\, h^3}{12\,(1-\nu^2)} \qquad d_2 = \frac{E\, h_r^3}{12\,(1-\nu^2)} \tag{23}$$

2.3.5. Configuration 3: Rib ≡ Beam

This configuration models the rib as a beam placed on top of the base plate (Fig. 1.3).

The kinetic energy of the system is evaluated as a superposition of both the base plate and the top beam.

$$T = \frac{1}{2}\left(\int_0^a \int_0^b \rho_1 \cdot \dot{w}^2 \, \mathrm{d}y \, \mathrm{d}x + \int_0^b \rho_2 \cdot \dot{w}\left(t, \frac{a}{2}, y\right)^2 \, \mathrm{d}y\right) \tag{24}$$

Here $\rho_1 = \mu h$ and $\rho_2 = \mu h_r$.

Likewise, for the potential energy.

$$V = \frac{1}{2}\left(\int_0^a \int_0^b d_1 \cdot W_V \, \mathrm{d}y \, \mathrm{d}x + \int_0^b EI_r \cdot w_{yy}\left(t, \frac{a}{2}, y\right)^2 \, \mathrm{d}y\right) + V_S \tag{25}$$

Where $I_r = L_r h_r^3 / 12$ is the rib's second moment of area.

2.3.6. Trial functions

Harmonic trial functions are the natural choice for simply supported boundary conditions, being the exact solution of the mode-shapes for rectangular flat plates. Since the rectangular ribbed plate is essentially a mutated flat plate, assuming harmonic functions serve as powerful elementary blocks and are conceptually a "good guess". Since no penalty method is used to provide simply supported boundary conditions, then $V_S = 0$ as there is no need for hypothetical springs. Harmonic trial functions can be used as:

$$\phi_{i,j}(x, y) = \sin\left(\frac{\pi \, x \, i}{a}\right) \sin\left(\frac{\pi \, y \, j}{b}\right) \tag{26}$$

Penalty methods, detailed in [17], are an interesting alternative of providing more flexibility in the definition of the boundary conditions and a way to increase computational efficiency by using simpler trial functions. The task is to model the plate with free edges sporting massless springs of preset stiffness k. By setting $|k|$ to be very large (e.g. of order E^{10}), the springs become stiff enough to simulate simply-supported boundary conditions. It is important to note that the magnitude must be large, but k is generally taken to be negative. Another crucial note is that penalty methods suffer from numerical instability. It is expected that the model can behave erratically for increasing values of n and for larger frequencies.

Polynomial trial functions offer the greatest improvement in efficiency being computationally simple (i.e. are easy to manipulate, differentiate, integrate, etc.). Individual trial functions can be defined as bivariate polynomials:

$$\phi_{i,j}(x, y) = \left(\frac{x}{a}\right)^{i-1} \left(\frac{y}{b}\right)^{j-1} \tag{27}$$

The massless (no kinetic energy) springs must be provided for as potential energy, such that

$$V_S = \frac{1}{2}\int_0^b k\left[w^2(t, 0, y) + w^2(t, a, y)\right] dy + \frac{1}{2}\int_0^a k\left[w^2(t, x, 0) + w^2(t, x, b)\right] dx \tag{28}$$

2.4 Experimental modal analysis

To calibrate the analytical and numerical models, validate their correctness, accuracy, and precision, and optimize them to reality as closely as possible, there was a need to acquire real-world data on a physical ribbed plate. A rectangular ribbed plate was fabricated on which experiments could be carried out. The selected material was 6061-T6 aluminum alloy for its availability and ease of machining. While aluminum can exhibit anisotropic behavior, it is sufficiently isotropic for the purpose of modal analysis of small deflections. Indeed, its properties are much more homogenous when compared to other common materials such as wood. An analog milling machine was used to reduce a thick rectangular slab of the alloy into a thin ribbed plate. The ribbed plate was dimensioned to $(\mathbf{206.00 \times 186.00 \times 2.15})\ \mathbf{mm^3}$ for the base plate, and to $(\mathbf{4.36 \times 186.00 \times 7.40})\ \mathbf{mm^3}$ for the rib. Two separate modal analysis experiments were carried out: the impulse hammer experiment, and the Chladni pattern method. Each has its own benefits and inconveniences, as will be compared in the results. Both experiments require fixing the plate, using Seal 'N Peel removable sealant, with as minimal plate-frame contact as possible. This is to reduce clamping effects and to approach simply-supported boundary conditions. A description of the experimental plate setup is provided in Fig. 3 and Table 1.

2.4.1. Impulse hammer modal testing

With the plate and frame properly set up, the impulse test consists of impacting the plate surface and measuring both the impact force using a load cell and the response using accelerometers. The signals are then fed through a signal conditioner and DAQ device into a computer for processing and modal extraction.

Table 1
Items used in the experimental setup of the impulse hammer test.

Item	Specifications
(1) Sealant Gun	Reduces plate-frame contact and minimizes clamping effects.
(2) Glue Gun	Fixes the accelerometers on the plate surface.
(3) Accelerometers	PCB PIEZOTRONICS INC. Model 352C22 SN LW244026.
(4) Plate and Frame	Simply-supports the plate and fastened with a wrench.
(5) Impact Hammer	KISTLER Model 9928 – Provides impacts and measures the force.
(6) Signal Conditioner	PCB PIEZOTRONICS INC. Model 482C Series.
(7) Power Supply/Coupler	KISTLER Type 5114 – Powers hammer and outputs signal.
(8) Multifunction I/O Device	NI USB-6212 – DAQ outputs to computer for processing.

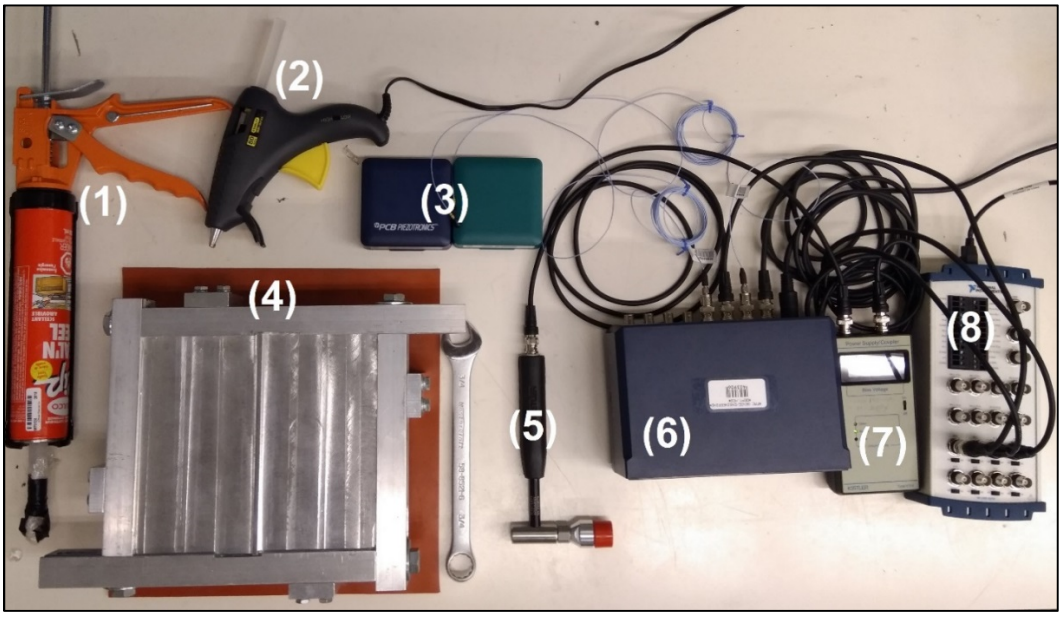

Fig. 2. Experimental setup for the impulse hammer test.

2.4.2. Ideal impulse hammer setup

Identifying the ideal setup required experimenting with various controlled parameters: boundary conditions (amount of sealant), angle and intensity of impact, pattern of impact (single versus multiple hits), and accelerometer positioning. After experimenting with varied setup parameters across 10 different trials, the ideal conditions for recording the impacts were identified. The plate should be fixed onto the frame with generous amounts of sealant, but not enough to leak onto the plate surface. This reduces clamping and is closest to simply-supported boundary conditions. A simple way to check correct fixture of the plate is to tap its surface and judge its sound and feel. It must not make metal-to-metal contact with the frame, but should flex freely. The hammer should have a perfectly orthogonal impact angle and the force range should be restricted from 25 to 65 N. The accelerometers should be placed at the $(1/4, 1/4)$ and $(3/4, 3/4)$ of the overall plate dimensions. This ensures that they avoid nodal lines of the mode-shapes of interest. Strikes should be single hit, at $(3/4, 1/4)$ and $(1/4, 3/4)$ of the overall dimensions, bi-opposite to the two accelerometers. Fig. 4 demonstrates the correct accelerometer (+) and impact (×) positions on the ribbed plate. These routines ensure the cleanest recording.

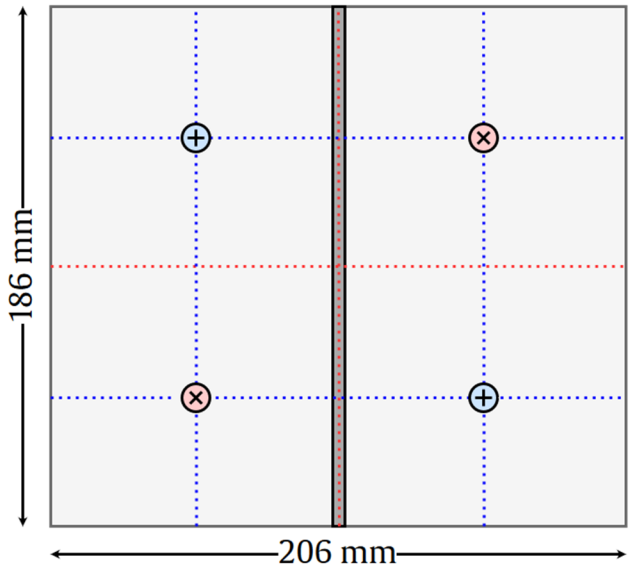

Fig. 3. Ideal positions for accelerometer placement (+) and hammer impact (×).

2.4.3. Impulse hammer signal processing

The DAQ is interfaced with MATLAB for real-time data recording, signal processing and isolation. Each of the accelerometer and impulse hammer signals should be isolated. The script uses logarithmic decrements for modal analysis, converting impulse and accelerations into natural frequencies. To compute the modal parameters, the Least-Squares Complex Exponential (LSCE) algorithm was found to be best suited for this experiment. This method is well-explained in [19] and is a natively available argument in MATLAB. It was also found to be more accurate to process displacement rather than acceleration. The window size (range of data points recorded on impact) must be optimized to obtain the cleanest results. A total of 100 data points was recorded. To avoid common recording mistakes: (1) ensure the load sensor is placed correctly on the impulse hammer, (2) verify by touch and sound that the plate is properly simply-supported, (3) test various window sizes, settings, and thresholds until the best combination is found, (4) when averaging, correctly reparse the i-th frequencies as they are generally not recorded sequentially.

2.4.4. Chladni pattern method

Starting from the same plate-frame setup, finely divided material, such as cake sprinkles, are sprinkled on the plate, under which is placed a sufficiently-powerful sound emitter. Computer-generated sine waves are amplified and emitted below the plate, which vibrates

and displaces the sprinkles. The speaker, placed at 3 mm from the underside of the plate measured from the top of its peripheral, emits sound at 40 W. A receiver measures acoustic sound intensity while the sine wave frequencies are swept. A natural frequency is reached when the receiver displays a local maximum value and when the sprinkles assume a Chladni pattern. These patterns expose the different mode-shapes by allowing the sprinkled material to accumulate at the nodal lines. The setup is described in Fig. 5 and Table 2.

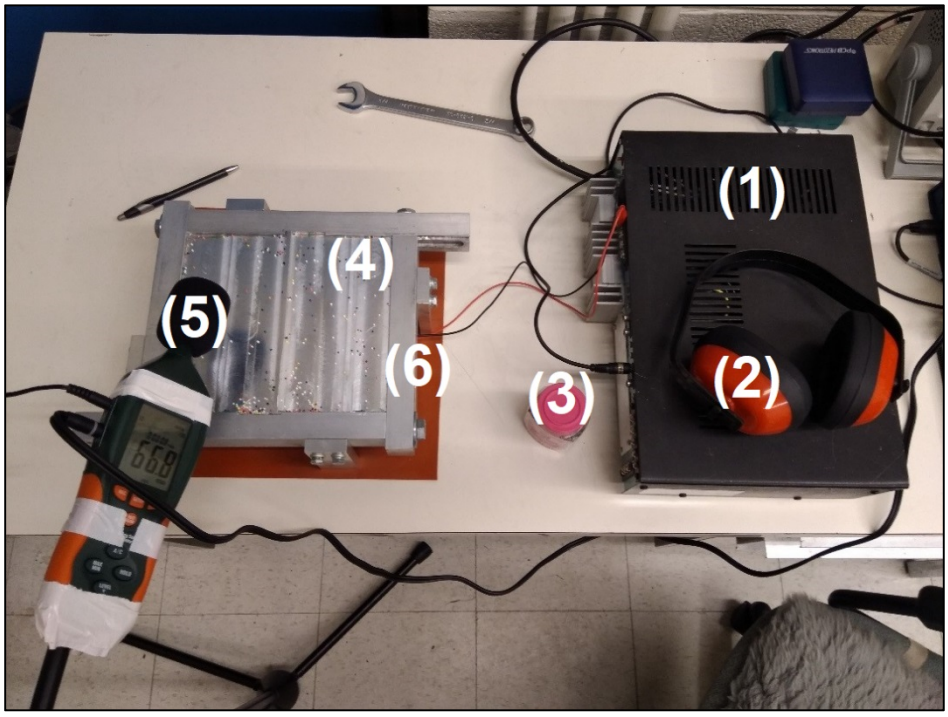

Fig. 4. Experimental setup for the Chladni patterns test.

Table 2
Items used in the experimental setup of the Chladni patterns test.

Item	Specifications
(1) Signal Amplifier	BOGEN Classic C60 Amplifier - 60 W RMS.
(2) Acoustic Earmuffs	Protects the subject from the loud generated sounds.
(3) Cake Sprinkles	Moves along with the mode-shapes being light and non-adhesive.
(4) Plate and Frame	Joined using a removable sealant and fastened with a wrench.
(5) Sound Receiver	EXTECH HD600 Datalogging Sound Level Meter.
(6) Sound Emitter	Diameter 5.5", nominal 50 W, maximum 120 W, impedance 8 Ω.

3. Results

3.1. Plate parameters

The parameters used in all the models described in section 2 were those of the physical plate used in the experiments. The geometric dimensions and the material properties of the ribbed plate are listed in Table 3. All derived parameters can be obtained from the listed inputs and are thus omitted. Material properties of 6061-T6 aluminum alloy are obtained from [20].

Table 3
Geometric dimensions and material properties of the ribbed plate.

Parameter		Values
a	Plate length (m)	$2.06 \cdot 10^{-1}$
b	Plate width (m)	$1.86 \cdot 10^{-1}$
E	Young's modulus (Pa)	$6.89 \cdot 10^{-10}$
h	Plate thickness (m)	$2.15 \cdot 10^{-3}$
h_r	Rib thickness (m)	$7.40 \cdot 10^{-3}$
k	Massless springs stiffness (N m^{-1})	$-1.00 \cdot 10^{10}$
L_r	Rib length (m)	$4.36 \cdot 10^{-3}$
μ	Volumetric mass density (kg m^{-3})	$2.70 \cdot 10^{-3}$
ν	Poisson's ratio	$3.30 \cdot 10^{-1}$

3.2. Experimental results

In the impulse hammer test, 100 data points were recorded, processed, and then averaged to yield the first five natural frequencies (f) and their corresponding damping ratios (ζ). All averages and corresponding standard deviations are listed in Table 4. In addition, the Chladni pattern method measured the first four natural frequencies, included in the same table.

Table 4
Natural frequencies and damping ratios obtained from the impulse hammer and Chladni patterns tests.

Experiment	1	2	3	4	5
$\bar{f}_{\text{impulse}}$ (Hz)	356.6	680.9	1,056	1,158	1,226
σ_f	2.423	3.049	2.855	2.652	2.559
$\bar{\zeta}_{\text{impulse}}$	0.0545	0.0418	0.0194	0.0580	0.0272
σ_ζ	0.0410	0.0302	0.00727	0.0310	0.0121
f_{Chladni} (Hz)	355.0	680.0	1,062	1,156	–

3.2.1. Measurement errors

The plate dimensions a and b were measured with an error of ± 0.5 mm equivalent to a relative error of approximately $\pm 0.25\%$. Since accelerometer measurement errors depend on too many factors, error bounds are difficult to quantify. However, it is possible to estimate an upper bound for the total error. In the impulse hammer experiment, even though the high-precision sensors were designed to produce highly-accurate results, they still required calibration. The calibration for both the hammer load sensor and the accelerometers carried some error. Moreover, the signal processing, while highly-optimized, also carried its own errors. In the Chladni pattern experiment, the room for error was much greater mainly because the measurement devices used were less precise and less accurate. Additionally, this experiment requires error-prone human readings of patterns to identify when resonance has been achieved. Using conservative estimates, the frequency values given by the impulse hammer experiment exhibit no worse than $\pm 1\%$ relative error, while those for the Chaldni pattern experiment are deduced relative to the impulse hammer test in Table 10.

3.3. Numerical model results

The FEA base model simulates the ribbed plate as is, while the augmented model adds two point-masses accounting for the weights and locations of the accelerometers on the plate, as in Fig. 4. These added masses have the effect of lowering the natural frequencies. Results for the models are listed in Table 5.

Table 5
First six natural frequencies obtained from base and augmented FEA models.

FEA Model	f_1 (Hz)	f_2 (Hz)	f_3 (Hz)	f_4 (Hz)	f_5 (Hz)	f_6 (Hz)
Base	357.7	684.3	1,064	1,169	1,229	1,905
Augmented	356.9	681.1	1,056	1,158	1,226	1,900

In addition, the mode-shapes for the base model are provided in Fig. 6. While these were obtained from the FEA model, they remain the same for all models discussed herein.

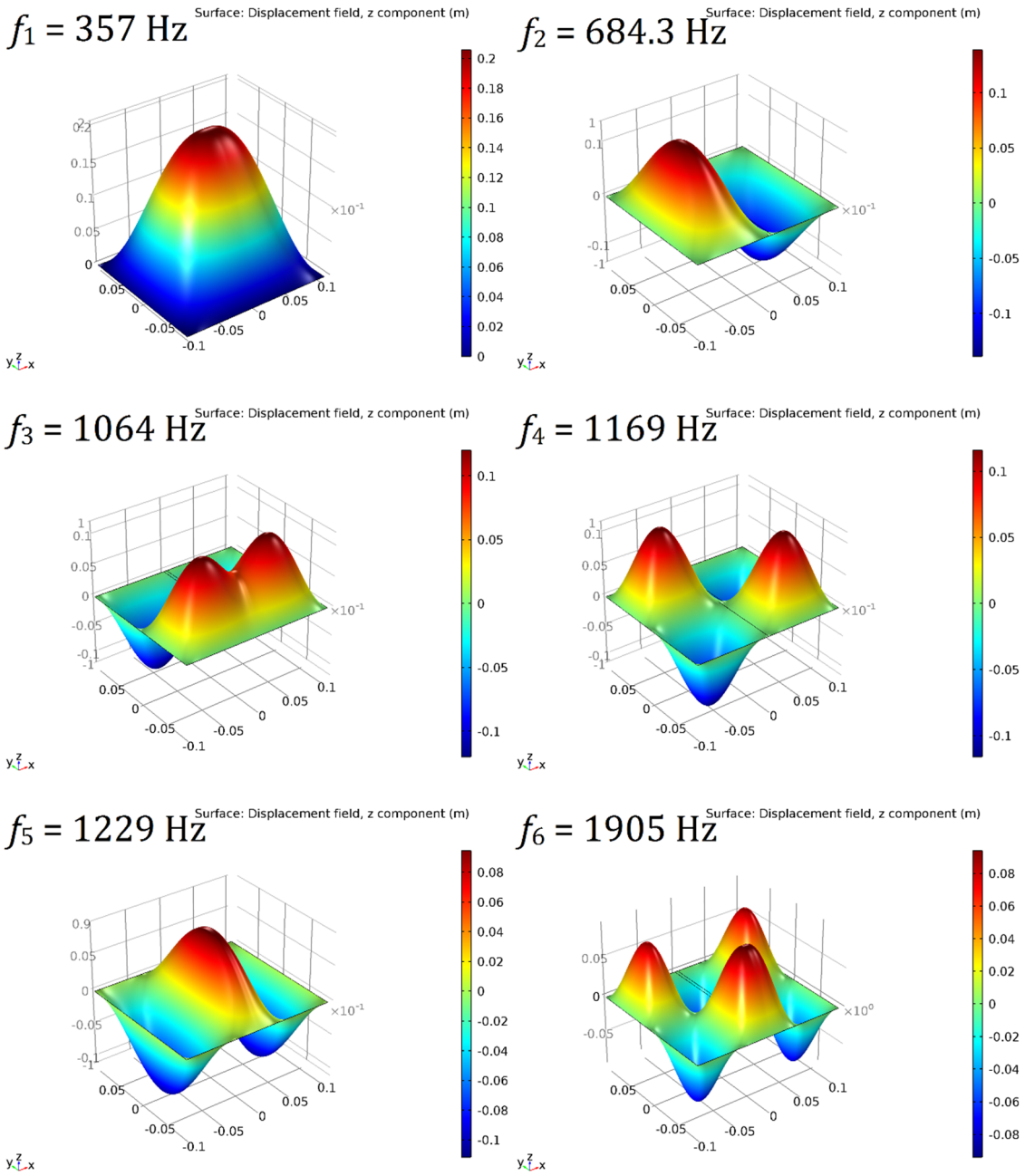

Fig. 6. First six mode-shapes of the ribbed plate obtained from the FEA base model.

3.4. Analytical model results

The first six natural frequencies using harmonic trial functions are listed in Table 6, with an increasing number n^2 of trial functions for different configurations.

Table 6
First six natural frequencies for different numbers of trial functions obtained from the three configurations.

Config.	n	n^2	f_1 (Hz)	f_2 (Hz)	f_3 (Hz)	f_4 (Hz)	f_5 (Hz)	f_6 (Hz)
1	5	25	365.9	822.5	1,093	1,362	1,534	2,035
	10	100	361.2	797.1	1,089	1,294	1,363	1,978
	15	225	359.6	795.9	1,082	1,291	1,296	1,942
	25	625	358.9	794.9	1,077	1,263	1,288	1,929
2	5	25	322.5	747.6	935.3	1,281	1,477	1,852
3	5	25	309.5	642.6	935.1	1,095	1,194	1,745

A property of the assumed-modes method is that solution values of frequency will decrease as n grows larger, therefore, not only are most of the solutions of configurations 2 and 3 less accurate than those of 1, but they will also get worse, as most of them start below those of the FEM reference values and will continue to decrease as n grows. Since configuration 1 is proven superior, it will be adopted for the remaining AMM results.

Similarly, the solutions of the polynomial penalty method (using configuration 1) are listed in Table 7. The symbol ℂ indicates a rejected complex solution.

Table 7
First six natural frequencies for different numbers of trial functions obtained from the penalty method.

n	n^2	f_1 (Hz)	f_2 (Hz)	f_3 (Hz)	f_4 (Hz)	f_5 (Hz)	f_6 (Hz)
5	25	425.7	902.6	1,415	1,639	2,132	2,831
10	100	370.3	816.8	1,092	1,357	1,725	2,038
12	144	365.9	815.9	1,092	1,352	1,542	2,036
13	169	706.4	811.1	1,092	ℂ	1,336	2,053
15	225	ℂ	807.6	1,092	ℂ	1,337	ℂ
16	256	333.2	807.2	1,092	1,336	ℂ	ℂ
25	625	813.2	910.8	ℂ	ℂ	1,090	1,322

3.5. Analytical model implementation

The analytical models were implemented on Wolfram Mathematica 11 and Maple 2017.

3.5.1. Parallelization and concurrency

The CPU used is an Intel Core i7-7700 with a clock-speed of 3.60GHz, 4 cores, and 8 logical processors. A serial implementation would run only on a single logical processor with idle time on variables waiting for prerequisite operations to complete. The Wolfram Language contains built-in parallel computing packages that allow the use of multiple Wolfram Kernels, i.e. multiple instances of Mathematica, to complete tasks concurrently and in parallel, fully exploiting the CPU. Using these built-in functions, the entire model is programmed in a parallel structure, outlined in Fig. 7. The grouped rectangular blocks run concurrently, while the circular ones are run necessarily in series. Each block is parallelized, when possible, across the 8 kernels. Conditional logic manages blocks to wait for prerequisite variables to complete evaluation. The result is the dependency network shown as the color-coded branches. The green blocks indicate the sequence taken to evaluate the elastic potential energy, and is skipped when the penalty method is not used. After migrating to a parallel structure, CPU usage went from 16% to 100% across all logical processors. Common strategies for parallelization and concurrency are outlined in [21].

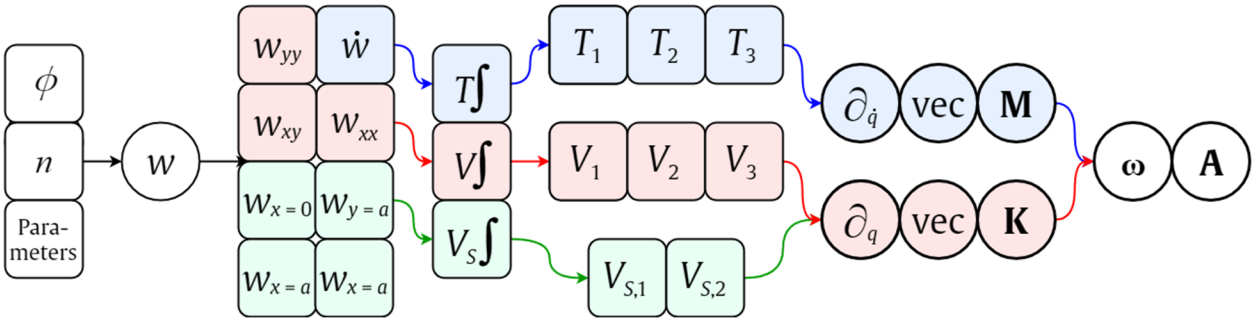

Fig. 7. Parallel and concurrent structure for the analytical model implementation.

3.5.2. Performance optimization

Optimizations in the parallel implementation are of two types: either mathematical constraints and operational simplifications, or faster algorithms for computationally-demanding mathematical operations. In the first type, constraining the model to the real domain skips the unnecessary computation of complex solutions, if detected. Moreover, computer algebra systems (CAS) software often have their own subroutines for symbolic integrations, which if the form of the integral is known, are futile checks. Since real elementary functions are being integrated in real domains, the second fundamental theorem of calculus suffices. Antiderivatives $\Psi(t)$ of functions $\psi(t)$ are first computed, and then set to

be evaluated at the integration bounds giving $\int_{t_1}^{t_2} \psi(t)\,\mathrm{d}t = \Psi(t_2) - \Psi(t_1)$. Additionally, before any symbolic integration is carried out, the integrand expressions should be simplified or expanded, using the CAS built-in algebraic transformations (e.g. Mathematica's **`FullSimplify[]`** and **`ExpandAll[]`**). This preprocessing step allows for faster integrations. In the second optimization type, by logging the duration spent on every operation, the two bottlenecks in the program are found to be the integrations and the eigensystem. Any further speedup requires efficient and parallel algorithms for these bottlenecks. For the eigensystem, there is an extremely useful property which can be exploited: **M** and **K** are both real-valued and symmetric, making them Hermitian matrices. The highly-parallel Lanczos algorithm is used to transform the $n_0 \times n_0$ Hermitian matrices into $n_1 \times n_1$ tridiagonal matrix, where $n_1 \leq n_0 \in \mathbb{N}$ allowing the approximation of the first n_1 eigenvalues (best accuracy is achieved for $n_1 = n_0$). The parallel QR algorithm is the principal eigensystem solver, but is not remarkably efficient with general matrices running in $\Theta\left(n^3\right)$. However, given symmetric matrices preprocessed into tridiagonal form, which is the role of Lanczos iterations, the QR algorithm scales linearly in $\Theta(n)$. The implementation details of these numerical linear algebra algorithms are described in [22]. Finally, the symbolic integrations use the parallel Risch-Norman (RN) algorithm, being more efficient for transcendental elementary functions (such as $\sin$) and especially suitable for trigonometric functions [23].

3.5.3. Time complexity

$T(m)$ is defined as the running time in seconds where the input $m = n^2$ is the total number of trial functions. The assumed-modes method is implemented as a process $\mathrm{amm}(\phi, m)$ which is composed of the numerical process $\mathrm{num}(m)$ and the symbolic process $\mathrm{sym}(\phi, m)$. All details pertaining to algorithmic analysis are clarified in [24]. By, suppressing constant factors and lower-order terms, the slowest symbolic computation sequence affected by the choice of trial function ϕ is in the potential energy. The following operation sequence is obtained.

$$\mathrm{sym}(\phi, m) \coloneqq \mathrm{integrate}^2 \circ \mathrm{square} \circ \mathrm{grad}^2 \circ \mathrm{sum}^2(\phi, m) \tag{29}$$

More explicitly,

$$\mathrm{sym}(\phi, m) \coloneqq \iint_{\Omega} \left[\left(\frac{\partial^2}{\partial x^2} + \frac{\partial^2}{\partial y^2} \right) \cdot \sum \sum \phi_{i,j}(x, y)\, q_{i,j} \right]^2 \mathrm{d}y\, \mathrm{d}x \tag{30}$$

Clearly, selecting harmonic functions would apply increased computational weight on the model, whereas polynomials would immensely simplify the flow of operations. The running time of the symbolic process is $T_{\text{sym},\phi}(m) = 2T_{\text{integrate},\phi}(m) + T_{\text{square},\phi}(m) + 2T_{\text{grad},\phi}(m) + 2T_{\text{sum},\phi}(m)$. The remaining operations of $\text{amm}(\phi, m)$, dependent only on m, are in $\text{num}(m)$. They are a composition of the vectorized (vec) derivative matrix (diff), with the eigensystem solution (eigen). The following statements define the processes.

$$\text{num}(m) \coloneqq \text{eigen} \circ \text{vec} \circ \text{diff}(m) \implies T_{\text{num}}(m) = T_{\text{eigen}}(m) + T_{\text{vec}}(m) + T_{\text{diff}}(m) \tag{31}$$

$$\text{amm}(\phi, m) \coloneqq \text{num} \circ \text{sym}(\phi, m) \implies T_{\text{amm},\phi}(m) = T_{\text{num}}(m) + T_{\text{sym},\phi}(m) \tag{32}$$

As stated earlier, the QR algorithm runs in linear time, therefore $T_{\text{eigen}}(m) \in \mathcal{O}(m)$. However, the Risch-Norman symbolic integration procedure is proven in [25] to belong to the **#P-complete** complexity class. Therefore, no worst-case running time can be deduced. Since, in this case, the input is the total number of trial functions, then a superlinear function $g(m) > m$ is assumed such that $T_{\text{integrate},\phi}(m) \in \mathcal{O}\big(g(m)\big)$. Since $\text{integrate}(\phi, m)$ and $\text{eigen}(m)$ are the highest-order processes in $\text{sym}(\phi, m)$ and $\text{num}(m)$, respectively, then $T_{\text{num}}(m) \in \mathcal{O}(m)$ and $T_{\text{sym},\phi}(m) \in \mathcal{O}\big(g(m)\big)$. For increasingly larger inputs, the integration procedure is measured to be the slowest part of the program. Therefore, $T_{\text{amm},\phi}(m) \in \mathcal{O}(\max\{m, g(m)\}) = \mathcal{O}\big(g(m)\big)$. There is no clear way to formally deduce the worst-case time complexity, but it can be estimated empirically. Since the number of trial functions used in practice never reach asymptotic proportions, performing a global asymptotic analysis is not crucial. Using benchmarks, it is possible to approximate $g(m)$ and the local order of growth through empirical analysis. Running times were recorded for $n \in [1, 25]$ for both the polynomial and harmonic trial functions. Table 8 lists the running times when polynomial trial functions are used.

Table 8
Running times of the analytical model polynomial implementation for different numbers of trial functions.

n	m	$T_{\text{amm,poly}}(m)$	n	m	$T_{\text{amm,poly}}(m)$	n	m	$T_{\text{amm,poly}}(m)$	n	m	$T_{\text{amm,poly}}(m)$
1	1	0.13	8	64	12.05	15	225	118.38	22	484	776.14
2	4	0.17	9	81	14.34	16	256	160.66	23	529	1,054.89
3	9	0.45	10	100	20.49	17	289	202.98	24	576	1,443.75
4	16	1.25	11	121	30.12	18	324	272.04	25	625	2,000.79
5	25	2.55	12	144	43.27	19	361	351.69	–	–	–
6	36	7.21	13	169	61.54	20	400	461.58	–	–	–
7	49	8.11	14	196	83.27	21	441	615.33	–	–	–

The data is plotted in both a linear (Fig. 8) and a log-log graphic (Fig. 9). The red plot is the segment-joined list plot of the tabular data and the orange dotted line is its monomial regression $T_{\text{reg,poly}}(m) = 10^{-2.999} \cdot m^{2.186}$ (appearing as a linear regression in the log-log plot). The blue plot ($T_{\text{fit,poly}}(m) = 6.650 \cdot m^{3.400} + 22.84$) is a polynomial curve fit modified to grow faster than the tabulated running time.

The red plot in the log-log graph appears increasingly linear for larger values of m, which suggests that assuming a polynomial profile for it is feasible. This is because polynomials of the form $T_p(m) = a_0 + \cdots + a_p m^p$ with $a_p > 0$ converge in the log-log plot to the oblique asymptote $\log_{10} T(m) = p \log_{10}(m) + \log_{10} a_p$, since $\lim_{m\to\infty} T_p(m) = \lim_{m\to\infty} a_p m^p$. The local order of growth is thus assumed to be polynomial with worst-case running time of $\mathcal{O}(m^{3.4})$.

Similarly, Table 9 lists the running times when harmonic trial functions are used.

Table 9
Running times of the analytical model harmonic implementation for different numbers of trial functions.

n	m	$T_{\text{amm,harm}}(m)$	n	m	$T_{\text{amm,harm}}(m)$	n	m	$T_{\text{amm,harm}}(m)$	n	m	$T_{\text{amm,harm}}(m)$
1	1	0.53	8	64	45.84	15	225	445.78	22	484	3,292.42
2	4	0.65	9	81	54.40	16	256	653.78	23	529	4,111.42
3	9	1.75	10	100	81.06	17	289	855.69	24	576	5,746.42
4	16	5.23	11	121	122.29	18	324	1,064.49	25	625	7,869.55
5	25	9.83	12	144	172.15	19	361	1,432.21	–	–	–
6	36	29.97	13	169	231.48	20	400	1,931.78	–	–	–
7	49	33.41	14	196	339.80	21	441	2,480.96	–	–	–

The running times have similar local order of growth patterns regardless of the trial function used and can be empirically assumed to be $\mathcal{O}(m^{3.4})$, however the actual running time differs. Effectively, the average ratio of the harmonic over the polynomial running times rounds up to 4, as shown below.

$$\mu_{\text{harm/poly}} = \frac{1}{25}\sum_{n=1}^{25}\frac{T_{\text{amm,harm}}(n^2)}{T_{\text{amm,poly}}(n^2)} \approx 4 \tag{33}$$

$$s_{\text{harm/poly}} = \sqrt{\frac{1}{24}\sum_{n=1}^{25}\left(\frac{T_{\text{amm,harm}}(n^2)}{T_{\text{amm,poly}}(n^2)} - \mu_{\text{harm/poly}}\right)^2} \approx 0.15 \tag{34}$$

Since the sample standard deviation is low, it can be empirically assumed that $T_{\text{amm,harm}}(n) \approx 4T_{\text{amm,poly}}(n)$.

Prior to parallelizing and optimizing, the inefficient serial implementation yielded $T \approx 3$ min for $m = 25$ instead of $T_{\text{amm,poly}}(25) = 2.55$ s and would render the software unresponsive for $m = 625$ instead of completing with $T_{\text{amm,poly}}(625) \approx 33$ min.

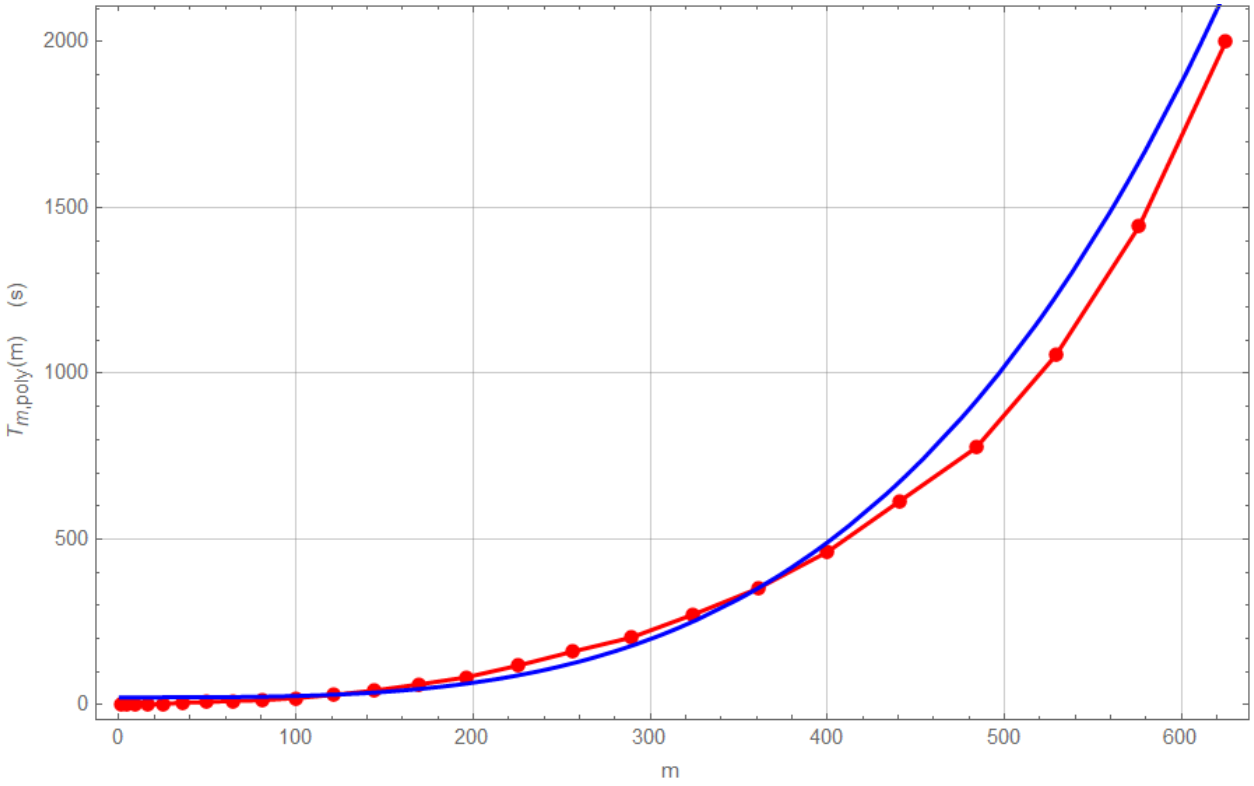

Fig. 8. Linear plot of the measured running time (red) and the modified polynomial curve fit (blue).

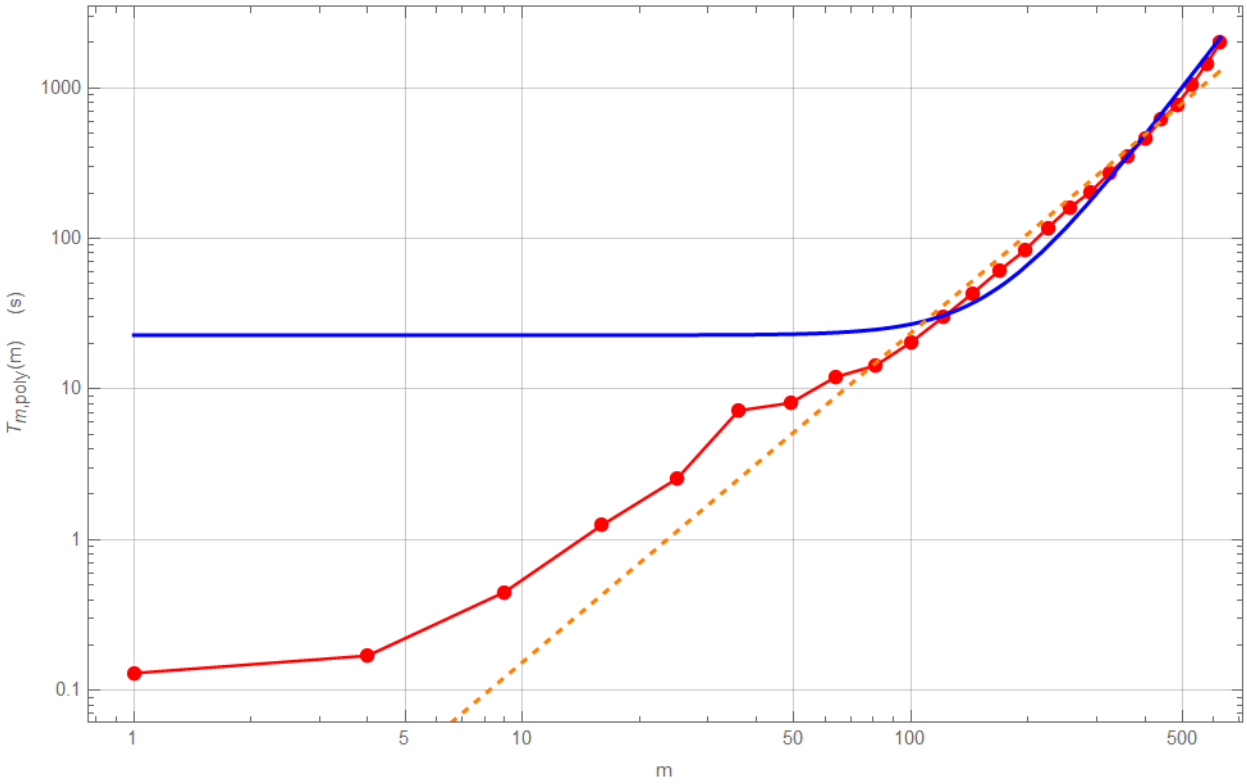

Fig. 9. Log-log plot providing the monomial regression (orange) of the running time (red).

4. Discussion

4.1. Comparison of the analytical and numerical models

4.1.1. Model accuracy

Let $\mathrm{err}_i(X) = 100 \cdot \left| f_{X,i} - f_{\mathrm{imp},i} \right| / f_{\mathrm{imp},i}$ be the percent error of method X relative to the impulse hammer experiment reference data, for every i-th natural frequency. Table 10 lists below the errors $\mathrm{err}_i(X)$ of every model and method in this study, the average error $\overline{\mathrm{err}}(X)$, and the error standard deviation $\mathrm{std}(X)$.

Table 10
Percent error of the natural frequencies given by each method relative to the impulse hammer results.

X Method	$\mathrm{err}_1(X)$	$\mathrm{err}_2(X)$	$\mathrm{err}_3(X)$	$\mathrm{err}_4(X)$	$\mathrm{err}_5(X)$	$\overline{\mathrm{err}}(X)$	$\mathrm{std}(X)$
FEA Model	0.30	0.49	0.73	0.98	0.21	0.53	0.29
Analytical (Config. 1, Harmon.)	0.64	16.74	1.99	9.07	5.06	6.70	6.48
Analytical (Config. 2, Harmon.)	9.56	9.80	11.43	10.62	21.47	12.38	4.59
Analytical (Config. 3, Harmon.)	13.2	5.62	11.45	5.44	2.61	7.67	4.46
Analytical (Config. 1, Polynom.)	2.61	18.55	3.41	15.37	8.97	9.78	7.09
Chladni Pattern Experiment	0.45	0.13	0.57	0.17	–	0.33	0.21

With an average error of less than 1%, the numerical model is the most accurate computational approach to determine the natural frequencies. Moreover, it is the only model that performs accurate computations for all frequencies, since it has an error standard deviation of 0.29. In comparison, all other models tend to determine some frequencies much more accurately than others, having large standard deviations, which is justified by the disparity in accuracy across different frequencies. Despite its relatively large average error, the analytical model using configuration 1 with harmonic trial functions can compute the fundamental frequency with only 0.64% error, the third partial with 1.99% error, and the fifth with 5.06%. However, it suffers problems with predicting the second and fourth frequencies which have considerably large errors. Note that this has nothing to do with odd versus even indexed frequencies, as the sixth frequency is within the neighborhood of the one computed by the FEA model. Rather, configuration 1 produces large errors for those frequencies which have a node line at the location of the rib. This implies that configuration 1 fails to accurately model the motion around a node line when a change in thickness occurs, which may be due to the limitations provided by Kirchhoff-Love plate theory. The two other configurations compute fundamental frequencies less accurately, having large errors of 9.56% and 13.2%. However, they seem to be more consistent across all frequencies. Nonetheless, this disqualifies them from further analysis in this study, since accurately computing the fundamental is an important and primary function of these models. Interestingly, Cho et al. demonstrate slightly better results using configuration 3 when using clamped boundary conditions, while simply supported results are similar [2-3]. Next, the effect of trial function selection on accuracy is compared. There is an expected superiority of harmonic functions because they are obtained from the solution of the vibrating flat plate. Moreover, the use of

polynomial penalty methods sacrifices accuracy for the sake of performance, and indeed as mentioned previously, it performs roughly 4 times faster but at half the accuracy. Using configuration 1, it also suffers from large errors in computing the second and fourth partial frequencies, similar to using harmonic trial functions. Alternatively, Monterrubio and Ilanko provide suggestions for alternative admissible trial functions which may help improve the accuracy of the penalty method [26-27].

4.1.2. Model stability

Besides comparing model accuracy, it is important to consider their stability, meaning the behavior of their convergence. The numerical model is robust and stable since it converges predictably (under adequate simulation configurations), and its errors decrease with decreasing mesh size. The analytical model stability will depend mainly on the choice of trial function. Selecting harmonic functions ensures predictable and stable behavior. The analytical model (configuration 1) in this study using harmonic functions always converges and its errors decrease as the number of trial functions is increased. The polynomial penalty method, however, exhibits unstable behavior when the number of trial functions is large enough (169 in this study, as in Table 7). First, the overall trend is that error decreases, but this is not deterministic as the error will sometimes sharply increase or even become infinite in the case of a complex solution. In fact, using more trial functions may result in an unstable solution at higher frequencies, while at lower frequencies there are no guarantees of convergence on acceptably accurate solutions. With that being said, the polynomial penalty method must be used with caution and must be compared to a stable reference when being designed and implemented.

4.1.3. Model performance

The numerical model is by far the fastest in computing the natural frequencies, since it discretizes the system and produces local solutions, which are then combined. It converges in fractions of a second. Certainly, increasingly finer meshes would require much more time, but within the scope of modal analysis, such detail is rarely required, and thus the FEA model remains the quickest in terms of convergence.

The analytical model performance, instead, will depend on more than one factor. Most importantly, the number of trial functions, which even after using highly-efficient parallel

algorithms, result in a local order of growth $\mathcal{O}(n^{3.4})$. This means doubling the number of trial functions will increase the running time by a factor of roughly 10.5 times. This is inevitably due to the highly demanding symbolic integrations. Moreover, the selection of trial functions will highly affect the actual running time, whereas the order of growth remains the same. As was previously demonstrated, using polynomial penalty functions render the model approximately 4 times faster, at the expense of being roughly 2 times less accurate.

However, this direct comparison is not entirely fair since the numerical model only generates discretized and local numerical solutions for a particular set of parameter values. The analytical model instead produces a continuous and global symbolic solution well-suited for parametric modification. It is possible to produce parametrized solutions, which can be utilized in programs to generate large arrays of data useful for studying the effects of individual or multiple parameters. In addition, and with some greater effort, it is possible to produce symbolic approximations in the form of parametric functions that could be used to create software libraries with pre-packaged symbolic solutions for ribbed plates. In comparison, the numerical model necessitates rerunning the simulation every single time to obtain the system description for a specific set of parameter values. The only way to run such operations programmatically is to perform parametric sweeps available within COMSOL. For these reasons, the analytical model does present some parametric advantages over the numerical one, despite having a much slower convergence time.

Finally, it is also important to compare model simplicity in terms of implementation and development. The analytical model is fairly complex, requiring the correct application of variational techniques for the core function. Moreover, optimizing the performance will require at least basic knowledge in parallel computation and the thorough implementation of specialized and highly-efficient parallel algorithms from numerical linear algebra.

4.2. Comparison of the impulse hammer and Chladni pattern methods

4.2.1. Method affordability

The impulse hammer experiment requires high-quality instrumentation and data acquisition (DAQ) hardware, including interfacing software capable of signal and data processing. Replicating the setup used in this study would cost between 4,000 and 5,000 USD. The Chladni pattern method is much cheaper to setup, well-under 1,000 USD.

4.2.2. Method simplicity

The method simplicity refers to the ease of setting up the experiment, and of running the experiment while also considering special procedures such as safety. The impulse hammer setup is fairly demanding, requiring proper fixture of the plate, and the correct connection and configuration of instrumentation and DAQ hardware. The most cumbersome part of the impulse hammer experiment is the signal and data processing of the accelerometer and load sensor outputs. The processing parameters require some trial-and-error sweeps before an ideal setting may be found, all of which can take up many hours. In comparison, the Chladni pattern experiment does not even require a computer, is fairly simple to setup and operate, but does require some safety measures. The sound generator can reach uncomfortable and even hazardous sound levels, which would require the added precaution of wearing protective hearing equipment.

4.2.3. Method accuracy

The impulse hammer method is by far the most accurate in this study, and the most repeatable once the setup and processing procedures are within ideal conditions. For these reasons, the impulse hammer experimental data has been chosen to be the reference data against which all other models and methods are compared. The Chladni pattern method achieved impressive levels of accuracy with all errors being well-under 1%. With an average error of 0.33% and a standard deviation of 0.21%, the accuracy is outstanding considering the cheap cost and ease of setup and operation of the Chladni pattern method.

4.3. Comparative summary of models and methods

Tables 11 and 12 summarize the advantages, disadvantages, and tradeoffs of each model or method used in this study.

Table 11
Summary of the advantages and tradeoffs of the studied ribbed plate models.

Model	Accuracy	Stability	Performance	Parametrization	Simplicity
FEA Model	●●●●●	●●●●●	●●●●●	●●○○○	●●●●●
Analytical (Config. 1, Harm.)	●●●●○	●●●●●	●●○○○	●●●●○	●●●○○
Analytical (Config. 2, Harm.)	●○○○○	●●●●●	●●○○○	●●●●○	●●●○○
Analytical (Config. 3, Harm.)	●○○○○	●●●●●	●●○○○	●●●●○	●●●○○
Analytical (Config. 1, Poly.)	●●●○○	●●○○○	●●●●○	●●●●○	●●●○○

It is important to note that it is difficult to deem one model or method as the inherent best, since the constraints of the application will determine the optimal method to select. It is easy to see the reasons why the FEA model is generally favored in the field, and especially in industry, because it is simply faster, more stable, more accurate, and simpler to implement. However, its limitations lead to a trial-and-error modal design approach.

Table 12
Summary of the advantages and tradeoffs of the studied experimental methods.

Method	Affordability	Simplicity	Accuracy
Impulse Hammer Experiment	●●○○○	●●○○○	●●●●●
Chladni Pattern Experiment	●●●●○	●●●●○	●●●●○

It is interesting to note that the Chladni pattern method is powerful when considering its costs and simplicity, and therefore can be used as a means to obtain low-frequency reference data when the expensive setup of the more reliable hammer method cannot be obtained.

5. Conclusion

This paper studied various analytical, numerical, and experimental approaches to the modal analysis of ribbed plates. Each method was characterized, implemented, and used to output its own set of natural frequencies. The assumed-modes method was applied to three different model configurations with two cases of trial functions. These different analytical models were measured against each other. As numerical packages are widely available as part of commercial simulation software, there was a special focus given to the implementation of the analytical models. Thorough specifications were given concerning the development,

parallelization, and optimization of the analytical package. Performance accelerations were achieved by fitting parallel and concurrent programming techniques wherever feasible. Mathematical simplifications yielded additional time savings, and high-performance parallel algorithms were exploited to reduce bottlenecks in the program. The favored analytical configuration was subjected to algorithmic analysis to estimate its local order of growth and empirically investigate its running time. The analytical models were directly compared to the numerical model, which employed finite element analysis. They competed in terms of accuracy, stability, ease of parametrization, and simplicity of implementation. In a similar fashion, the experimental modal analysis techniques were compared in their accuracy, cost, and ease of setup and operation. This comparative study exposes vibration scientists and engineers to possible modal analysis techniques based on their advantages and disadvantages, and allows them to select the approach most suitable for their research, application or design problem, but also offers a template onto which their specific uses may be layered.

References

[1] D.S. Cho, B.H. Kim, J.H. Kim, T.M. Choi, N. Vladimir, Free vibration analysis of stiffened panels with lumped mass and stiffness attachments, Ocean Eng. (2016). doi:10.1016/j.oceaneng.2016.07.055.

[2] D. Cho, N. Vladimir, T. Choi, Natural vibration analysis of stiffened panels with arbitrary edge constraints using the assumed mode method, Eng. Marit. Environ. 229 (2015) 340–349. doi:10.1177/1475090214521179.

[3] D.S. Cho, J.H. Kim, T.M. Choi, B.H. Kim, N. Vladimir, Free and forced vibration analysis of arbitrarily supported rectangular plate systems with attachments and openings, Eng. Struct. 171 (2018) 1036–1046. doi:10.1016/j.engstruct.2017.12.032.

[4] P. Dumond, N. Baddour, Effects of using scalloped shape braces on the natural frequencies of a brace-soundboard system, Appl. Acoust. (2012). doi:10.1016/j.apacoust.2012.05.015.

[5] T. Lin, J. Pan, A closed form solution for the dynamic response of finite ribbed plates, Acoust. Soc. Am. 119 (2006) 917–925. doi:10.1121/1.2146111.

[6] L. Dozio, M. Ricciardi, Free vibration analysis of ribbed plates by a combined analytical-numerical method, J. Sound Vib. (2009). doi:10.1016/j.jsv.2008.06.024.

[7] T.R. Lin, An analytical and experimental study of the vibration response of a clamped ribbed plate, J. Sound Vib. (2012). doi:10.1016/j.jsv.2011.10.013.

[8] W.G. Halvorsen, Impulse Technique for Structural Frequency Response Testing, Sound Vib. (1977). doi:10.1121/1.2016847.

[9] R.S. Minette, S.F. SilvaNeto, L.A. Vaz, U.A. Monteiro, Experimental modal analysis of electrical submersible pumps, Ocean Eng. (2016). doi:10.1016/j.oceaneng.2016.07.054.

[10] T.R. Moore, A.E. Cannaday, S.A. Zietlow, A simple and inexpensive optical technique to help students visualize mode shapes, J. Acoust. Soc. Am. (2012). doi:10.1121/1.3677244.

[11] D.S. Cho, B.H. Kim, J.H. Kim, N. Vladimir, T.M. Choi, Simplified dynamic analysis of stepped thickness rectangular plate structures by the assumed mode method, Eng. Marit. Environ. 231 (2016) 177–187. doi: 10.1177/1475090216630001.

[12] I. Shufrin, M. Eisenberger, Semi-analytical modeling of cutouts in rectangular plates with variable thickness – Free vibration analysis, Appl. Math. Model. (2016). doi:10.1016/j.apm.2016.02.020.

[13] H. Xu, J. Du, W.L. Li, Vibrations of rectangular plates reinforced by any number of beams of arbitrary lengths and placement angles, J. Sound Vib. (2010). doi:10.1016/j.jsv.2010.03.023.

[14] J.R. Wu, W.H. Liu, Vibration of rectangular plates with edge restraints and intermediate stiffeners, J. Sound Vib. (1988). doi:10.1016/S0022-460X(88)80081-6.

[15] M.K. Lee, M.H. Fouladi, S.N. Namasivayam, An analytical model for computing the sound power of an unbraced irregular-shaped plate of variable thicknessNo Title, Sci. Rep. 8 (2018). doi:10.1038/s41598-018-33645-y.

[16] C.R. Steele, C.D. Balch, Introduction to the Theory of Plates, Stanford Univ. (2009). doi:2012938665.

[17] L. Meirovitch, Fundamentals of Vibrations, 2001. doi:10.1115/1.1421112.

[18] L. Komzsik, Applied Calculus of Variations for Engineers, 2nd ed., CRC Press, 2008.

[19] W. Zhou, D. Chelidze, Generalized Eigenvalue Decomposition in Time Domain Modal Parameter Identification, J. Vib. Acoust. (2008). doi:10.1115/1.2775509.

[20] J.R. Davis, Metals Handbook, Met. Handb. (1998). doi:10.1017/CBO9781107415324.004.

[21] G. Hager, G. Wellein, Introduction to High Performance Computing for Scientists and Engineers, 2011. doi:10.1201/EBK1439811924.

[22] L.N. Trefethen, D. Bau III, Numerical linear algebra, Numer. Linear Algebr. with Appl. (1997). doi:10.1137/1.9780898719574.

[23] K. Geddes, L. Stefanus, On the Risch-Norman Integration Method and Its Implementation in MAPLE, Proceeding ISSAC ' 89 Proc. ACM-SIGSAM 1989 Int. Symp. Symb. Algebr. Comput. (1989) 212–217.

[24] C.C.E. Leiserson, R.R.L. Rivest, C. Stein, T.H. Cormen, Introduction to Algorithms, Third Edition, 2009. doi:10.2307/2583667.

[25] B. (KTH) Terelius, Symbolic Integration, (2009) 51–54, 69–73. https://www.nada.kth.se/utbildning/grukth/exjobb/rapportlistor/2009/rapporter09/terelius_bjorn_09095.pdf.

[26] S. Ilanko, L.E. Monterrubio, Y. Mochida, The Rayleigh-Ritz Method for Structural Analysis, 2014. doi:10.1002/9781118984444.

[27] L.E. Monterrubio, S. Ilanko, Set of admissible functions for the Rayleigh-Ritz method, in: B.H.V. Topping (Ed.), Elev. Int. Conf. Comput. Struct. Technol., Civil-Comp Press, 2012.